# A streamlined workflow for automated cryo focused ion beam milling

**Sebastian Tacke[1,4], Philipp Erdmann[2,4], Zhexin Wang[1], Sven Klumpe[2], Michael Grange[1], Radim Kříž[3], Matej Dolník[3], John Mitchels[3], Jürgen Plitzko[2,*], Stefan Raunser[1,*]**

[1]Department of Structural Biochemistry, Max Planck Institute of Molecular Physiology, Otto-Hahn-Str. 11, 44227 Dortmund, Germany

[2]Department Molecular Structural Biology, Max Planck Institute of Biochemistry, Am Klopferspitz 18, 82152 Martinsried, Germany

[3]Thermo Fisher Scientific, Materials & Structural Analysis, Vlastimila Pecha 1282/12, 62700 Brno, Czech Republic.

[4]These authors contributed equally

[*]Correspondence: stefan.raunser@mpi-dortmund.mpg.de, plitzko@biochem.mpg.de

## Abstract

Cryo-electron tomography (cryo-ET) is an emerging technique to study the cellular architecture and the structure of proteins at high resolution *in situ*. Most biological specimens are too thick to be directly investigated and are therefore thinned by milling with a focused ion beam under cryogenic conditions (cryo-FIB). This procedure is unautomated and prone to contaminations, which makes it a tedious and time-consuming process, often leading to suboptimal results. Here, we present new hardware and software tools that overcome the current limitations. We developed a new glove box and a high vacuum cryo transfer system and installed a stage heater, a cryo-shield and a cryo-shutter in the FIB milling microscope. This reduces the ice contamination during the transfer and milling process and simplifies the handling of the sample. In addition, we introduce a new software application that automates the key milling steps. Together, these improvements allow for high-quality, high-throughput cryo-FIB milling. This paves the way for new types of experiments, which have been previously considered infeasible.

## Introduction

Electron tomography at cryogenic temperatures (cryo-ET) offers the unique possibility to structurally analyse biological macromolecules in their native cellular environment [Grange2017, Bartesaghi2012]. Using this method, it is even possible to determine protein structures at near-atomic resolution by applying sub-volume averaging techniques [Schur2016].

One prerequisite for electron cryo microscopy is that the sample is thinner than the inelastic mean-free-path length of electrons (approximately 350 nm for 300 keV electrons [Vulovic2013]. Thicker samples result in an increased number of inelastically scattered electrons, which decreases the quality of the image. The majority of biological samples (e.g. eukaryotic cells or tissues) are too thick for cryo-ET and need to be thinned.

Cryo-ultramicrotomy is one approach that can be used to reduce specimen thickness. Here, the sample is cut into ribbons of vitreous sections that are thin enough to be imaged by cryo-ET [Al-Amoudi2004]. However, this method is technically demanding and prone to sample-altering artefacts such as knife marks, compression or crevasses [Al-Amoudi2005]. Another approach uses a focused ion beam under cryogenic conditions (cryo-FIB) in a scanning electron microscope (SEM) to thin samples [Marko2007, Rigort2010]. In recent years, numerous studies have demonstrated the suitability of this technique for preparing biological samples for cryo-ET without the artefacts known from cryo-ultramicrotomy [Hagen2015, Mahamid2016].

Current best-practice protocols for cryo-FIB milling include: i) vitrification of the sample, ii) identification of regions-of-interest, iii) rough ablation of the surrounding sample material and iv) polishing of the target region, leaving a thin lamella ready for cryo-ET [Medeiros2018]. However, the entire procedure involves multiple handling, transfer, milling and imaging steps. During these steps, samples need to be handled with forceps and it is difficult even for highly experienced practitioners not to destroy the thin and fragile lamellae. Moreover, since the vitrified sample needs to be cooled constantly to avoid de-vitrification, it is especially prone to any kind of ice contamination. Contamination of polished lamellae is particularly disruptive to cryo-ET as ice crystals often obscure the view on features otherwise visible in the lamellae. It is even possible that ice crystals conceal the entire lamella, which prevents any meaningful data acquisition (Figure 1a). Besides the transfer, which bears a high risk of exposing the sample to water, a potential source of (amorphous) ice contamination is

68 the cryo-FIB/SEM itself. Despite the high vacuum inside the SEM, water molecules from the
69 residual gas inside the microscope chamber can still deposit on the sample that is kept well
70 below -140 °C to avoid devitrification (Figure 1b). Depending on the partial pressure of water
71 inside the chamber, this effect can be severe and ultimately limits the number of lamellae that
72 can be prepared per session.

73 During the milling process, most of the steps to date need to be adjusted manually,
74 resulting in relatively long operator times at the cryo-FIB/SEM. Because of the lack of
75 automation, unattended overnight runs are currently not possible, limiting the total number
76 of preparations per week. Taken together, the highest throughput reported so far is limited
77 to 16 lamellae per session (10 hours) [Medeiros2018].

78 To obtain optimal lamellae for cryo-ET and to increase the overall throughput of cryo-
79 FIB milling, three major hurdles need to be overcome: First, all types of contamination need
80 to be reduced to a minimum, and anhydrous environments need to be established for the
81 handling and transfer of the sample. At the same time, surface contamination inside the
82 microscope needs to be decreased. Second, the handling of the lamellae must be improved
83 to avoid lamella cracking. Third, all steps for the production of the lamellae on the system
84 need to be automated in order to reduce heterogeneity and increase throughput.

85 Here, we present an integrated workflow that addresses and overcomes all three
86 bottlenecks. In a first step, we implemented a specially designed glove box and a high vacuum
87 cryo transfer system into the current workflow to reduce ice contamination during handling
88 and transfer. Secondly, we tremendously reduced the contamination rates inside the cryo-
89 FIB/SEM by the installation of a stage heater, a cryo-shield and a cryo-shutter. Thirdly, we
90 demonstrate that most of the milling steps can be automated by a new software application.
91 We show that in combination the new hardware and software increase the overall throughput
92 of lamella production, enabling new types of experiments, which are considered infeasible
93 with current setups.

94

95 # Results

96 **Sample preparation and handling**

97 After vitrification by plunge or high-pressure freezing, the EM grid with the sample is placed
98 into the Autogrid, then put into the Aquilos Autogrid shuttle and transferred to the cryo-
99 FIB/SEM. During these steps the sample needs to be kept at temperatures below -140˚C to

avoid hexagonal ice formation. Many cryo-EM laboratories have implemented air-dehumidifier rooms. While those help to reduce the overall humidity, and thereby ice contamination, they cannot completely prevent it.

To eliminate ice contamination during handling and simplify implementation of the technique in laboratories unable to control room humidity, we developed a glove box system (Figure 2a) that allows the grid preparation steps to be performed in a tightly regulated atmosphere. During operation, the glove box is constantly purged with dry nitrogen gas to keep the humidity below the detection limit (1 %) of the humidity sensors used. Beyond functionality, the glove box system was designed to provide maximal convenience during grid preparation. To guarantee that the sample can be brought into the box without disturbing the anhydrous environment inside, we equipped the glove box with a load lock and a port for a high vacuum cryo transfer system. The direct supply of liquid nitrogen is provided by a liquid nitrogen reservoir, which is located inside the glove box. Furthermore, we installed a set of heated tool holders in the box that allow to heat and dry different tools, such as forceps, clipping tools, cassette gripper, etc. directly after usage.

To increase the ease of handling grids inside the box, we designed and built a dedicated universal preparation station (Figure 2b), again maximising the convenience for the user. The station contains an isolated liquid nitrogen bath with three different preparation modules for each step of grid preparation, namely autoloader grid assembly, cryo-FIB shuttle loading and autoloader cassette loading. The users can arrange the needed modules according to their working routine.

To avoid contamination and devitrification during sample transfer from the plunge freezer to the glove box and from there to the cryo-FIB/SEM, we implemented a previously developed high vacuum cryo transfer system [Tacke2016] (Figure 2c), which consists of a transfer rod, a liquid nitrogen reservoir, a vacuum chamber, a valve and a plug & play adapter for the glove box or cryo-FIB/SEM. To avoid devitrification during transfer, the cryo-FIB shuttle is actively cooled by the liquid nitrogen reservoir as soon as the transfer rod is retracted in its parking position. Moreover, because the cooled surfaces of the nitrogen reservoir act as a cryo-pump, the vacuum level is kept constant as long as the reservoir is filled [Tacke2016].

With the introduced devices, we are able to minimise the artefacts, currently associated with existing workflows streamlining the entire grid preparation whilst improving user convenience, efficiency and flexibility. Especially during sample screening, where many

132 samples have to be prepared and transferred over a longer timeframe, the benefit of the
133 devices is apparent. Due to the reduced humidity, the preparation station can stay cooled for
134 several hours without ice contamination and the high vacuum cryo transfer system allows the
135 necessary quick and contamination-free transfer.
136
137
138 **Hardware modification of the cryo-FIB**
139 Although cryo-FIB/SEMs are typically operated at high vacuum conditions, contamination of
140 the sample inside the microscope cannot be completely avoided, due to various sources of
141 contamination in the FIB chamber. One of these is the ablated sample material which re-
142 deposits on the specimen. This kind of contamination is greatest at the beginning of lamellae
143 preparation when the sample material is milled in bulk and decreases to a minimum towards
144 the final polishing step. It is therefore not a major problem for the production of lamellae if
145 the milling is performed in two stages: first all sites are roughly milled to a thickness of
146 approximately 500 - 800 nm and only then the final thinning is performed.
147 The second source of contamination is residual water inside the vacuum chamber. Its
148 deposition/sublimation rate depends on two factors: i) the fraction of water in the residual
149 gas mixture (partial pressure) and ii) the surface temperature of the sample material
150 (Supplementary Figure 1a). We installed a large cryo-shield and a cryo-shutter to reduce the
151 partial pressure of water in the system to less than 3 x $10^{-9}$ mbar and heated the sample to
152 max. -165 ˚C using a newly installed stage heater (Figure 3). Combined, these actions moved
153 the ratio between deposition and sublimation closer towards an equilibrium, i.e. minimal
154 deposition rates, which is optimal for cryo-FIB milling (Supplementary Figure 1a) (see also
155 [Umrath1983], [Echlin1992]).
156 Due to the increased pumping speed, the partial pressure decreases from 2-3 x $10^{-7}$
157 mbar to approximately 3 x $10^{-9}$ mbar when the cryo-shield is cooled with liquid nitrogen. After
158 30 min, the system reaches the lowest partial pressure of water (Supplementary Figure 1b).
159 The cryo-shutter in the direct vicinity of the sample (Figure 3) reduces the partial pressure in
160 this position even further. Under these conditions the contamination rate is 5.6 ± 1.0 nm $h^{-1}$
161 in the milling position compared to 85 ± 7 nm $h^{-1}$ without these modifications (Supplementary
162 Figure 2, Supplementary Table 1). It should be mentioned, that the initial contamination rate
163 is different for each microscope. Typically, the contamination rate for the used cryo-FIB/SEM

164 is specified to be smaller than 50 nm $h^{-1}$. In combination, the improved vacuum conditions
165 allow for milling over a longer time course and pave the way for supervised automated milling
166 strategies.
167
168 **Automated lamella production pipeline**
169 The lamella production workflow can be separated in four major steps: i) definition of
170 region(s)-of-interest (ROI), ii) site preparation, iii) rough milling and iv) thinning
171 (Supplementary Figure 3). In this study, we used the software application MAPS (Thermo
172 Fisher Scientific) to visually identify ROIs directly in the cryo-FIB/SEM (Supplementary Figure
173 3a). If this is not possible or rare biological events, such as for instance cell-cell fusions, are
174 investigated, the correlation of light cryo microscopy and cryo-FIB/SEM is needed. After
175 defining the milling position, the eucentric height and the milling angle are set for each lamella
176 site. We then used the new software application AutoTEM Cryo (Thermo Fisher Scientific) for
177 the next steps. AutoTEM Cryo executes site preparation, rough milling and thinning in a
178 supervised or fully automated manner (Supplementary Figure 3b).
179 First, AutoTEM Cryo imports the list of lamella sites from the MAPS software and all
180 parameters relevant for milling, such as ion beam currents, dimensions of the initial milling
181 pattern, desired lamellae dimensions etc., are defined. Once set, the program saves all
182 relevant parameters in template files. This allows to mill future batches exactly under the
183 same conditions and thereby helps to improve the reproducibility of the process.
184 Furthermore, with the help of the defined templates, the milling process can be easily
185 optimized for different types of specimen.
186 After defining all relevant parameters, the automated milling process starts (Figure 4).
187 If two different materials are used during EM grid production (e.g. copper and carbon), the
188 stability of the fragile carbon layer might suffer during freezing due to the different expansion
189 coefficients of the two materials. During site preparation, the ROI is centered and thereafter
190 relief cuts are milled, to release the stress of the support layer (Figure 4a) [Wolff2019]. The
191 subsequent rough milling is divided into four steps (Figure 4b). First, the bulk material is
192 removed with relatively high ion beam currents (0.5 – 1 nA) until a lamella thickness of
193 approximately 2-3 µm is reached (Figure 4c). In the following three milling steps, the ion
194 currents are successively decreased from approximately 0.5 nA to 0.1 nA and the lamella
195 thickness is gradually reduced to approximately 150 - 250 nm (Figure 4c). To produce a

196 uniform thickness, the lamella is tilted by a few degrees prior to milling to compensate for the
197 ion beam divergence [Schaffer2017]. Finally, the lamella is polished with relatively low ion
198 beam currents (30 -50 pA) to obtain a thickness of 100 - 200 nm (Figure 4d).
199
200 **Efficiency estimation and quality assessment**
201 To estimate the efficiency of our lamellae preparation pipeline, that is the production
202 of thin and intact lamellae, we separated the handling steps into two parts: i) the pre-
203 processing and ii) the post-processing. The pre-processing includes the assembly of the
204 autoloader grid, its loading to the cryo-FIB shuttle and the transfer of the shuttle from the
205 glove box to the cryo-FIB. The post-processing step comprises the transport from cryo-
206 FIB/SEM to the glove box and the transfer of the autoloader grid from the cryo-FIB shuttle to
207 the autoloader cassette.
208 In recently published preparation protocols, the success rate of obtaining suitable
209 specimens for proficient users was estimated to be 80% for the pre-processing and 90% for
210 the post-processing step, which results in a total efficiency of 72% [Medeiros2018]. In reality,
211 the efficiency is probably even lower because some lamellae will not be usable for cryo-ET
212 analysis.
213 Our improvements of the pre-processing and post-processing steps resulted in a
214 considerably higher efficiency of above 95% for the entire handling (pre- and post-processing).
215 In addition, all intact lamellae were almost contamination free (Figure 5a) and only in rare
216 cases, ice crystals could be found in the vicinity of the lamellae. Importantly, since the
217 contamination inside the cryo-FIB/SEM was reduced to a minimum, almost no contamination
218 layer could be identified in the final tomograms (Figure 5b) and approximately 90% of all intact
219 lamellae were in principle useable for cryo-ET investigations. Taken together, the high
220 efficiency and low contamination rate reflect the impact of the newly implemented hardware
221 components.
222 To assess the quality of the automated lamellae preparation, we applied the same
223 approach as described above. We investigated different types of specimens and quantified
224 the success rates for the rough milling and polishing. We considered a milling task as
225 successfully terminated, if the following criteria were fulfilled: i) the lamella was intact, i.e. not
226 broken, ii) the desired thickness was reached, iii) tracking of the lamella site was successful,
227 i.e. the right position of the sample was milled. We determined an average success rate of

228 95% and 88% for the rough milling and polishing, respectively (Table 1). With the estimated
229 efficiency of 95% for the pre- and post-processing and the calculated efficiency of 84% for the
230 milling process, the efficiency of the total workflow can be estimated to be around 80%.
231 Although the success rate was much higher in the case of manual milling (above 95%), the
232 total throughput is much higher since overnight runs are possible at this point. Moreover, the
233 operator time is significantly reduced.

234 To demonstrate that lamellae, prepared by automated cryo-FIB milling using AutoTEM
235 cryo, are suitable for subtomogram averaging, a set of ribosomes were identified on several
236 lamellae (Figure 6a,b). With only 15,000 particles, a structure of 14 Å (0.143 FSC criteria) was
237 calculated (Figure 6c, e). Since the orientations and locations can be precisely determined, we
238 were able to identify polysomes (Figure 6d).

239 Taken together, these results clearly demonstrate that the streamlined workflow not
240 only increases the overall throughput of the lamellae production but also generates results
241 that are suitable for in-situ high-resolution investigations.

242

243

## 244 Discussion

245 Contamination of the samples, inconvenient sample handling and the lack of automation are
246 the three dominant bottlenecks of current cryo-FIB workflows, which can decrease the quality
247 of the final lamellae and limit the overall throughput per milling session. In the present study
248 we overcame the aforementioned limitations by the introduction of new hardware
249 components (Table 2) and a new software to automate milling procedures.

250 To reduce sample contamination throughout the entire preparation process, we
251 introduced a glove box and a cryo high vacuum transfer system. Moreover, we significantly
252 reduced the contamination rates inside the vacuum system, mainly because of the installation
253 of an additional cryo-shield and a cryo-shutter. Now, the entire handling and transfer steps as
254 well as the cryo-FIB milling can be performed in an almost anhydrous environment. In order
255 to streamline the handling of the grids carrying fragile lamellae, we introduced a new
256 preparation station, which aims at avoiding all types of artefacts related to sample handling
257 with maximal convenience for the user.

258 The contamination rate of 88 nm $h^{-1}$ in the initial cryo-FIB/SEM setup limited the total
259 number of prepared lamellae per session. Due to the improved and new hardware, we could

260 decrease the contamination rate to 5.6 nm $h^{-1}$ in the milling position. Therefore, the lamella
261 production is not restricted to a specific time frame anymore and, in principle, an 24/7
262 operation is possible now.

263 Since this is difficult to realize by manual operation, we introduced the new software
264 application AutoTEM Cryo, which successively processes the queue of lamella sites in a
265 supervised to automated manner, allowing for the automatic batch milling of many lamellae.
266 With the help of AutoTEM Cryo, the time spent on the microscope is now reduced to
267 approximately 5 minutes per lamella site at the beginning of the milling process. Because of
268 the automation of Aquilos cryo-FIB milling, we can now fully exploit the benefits of the
269 hardware improvements and can indeed process up to 28 lamellae per session. In addition,
270 the supervised automated milling process allows users to explore the influence of different
271 milling parameters and strategies in a systematic manner. Due to the higher throughput,
272 quality assessment routines can be developed and once these routines are established, the
273 influence of different milling parameters can more readily be investigated, for example the
274 influence of high ion currents (2-3 nA) on the quality of the cryo-lamella, which is not yet fully
275 understood.

276 Taken together, the combination of new hard- and software increases the overall
277 throughput of lamellae production, improves the quality of the lamellae, and simplifies the
278 process of cryo-FIB milling and sample transfer. In addition, the methods described in this
279 work enable new types of experiments, which were previously difficult to realize.

280

281 # Acknowledgements

282 We thank Roger Wepf for many fruitful discussions and the exchange of ideas. We also thank
283 Sagar Khavnekar and Florian Beck for help with subtomogram averaging. This work was
284 supported by funding from the Max Planck Society (to S.R. and J.P.). M.G. is supported by an
285 EMBO Long-Term Fellowship.

286

287 # Material and Methods

288 **Glove box, preparation station and cryo high vacuum transfer**

289 The glove box has been manufactured by Microscopy Solutions Py. Ltd and modified by us
290 accordingly. Before sample preparation, the glove box is purged overnight with dry nitrogen.
291 Before the sample is brought into the glove box through the load lock, the liquid nitrogen

292 reservoir and the preparation station are filled with liquid nitrogen. Then, EM grids are clipped
293 to the Autogrids, if not already done. Thereafter, the Autogrids are loaded into the cryo-FIB
294 shuttle and transferred to the Aquilos microscope via the cryo high vacuum transfer system.
295 After the milling session has started, both the glove box as well as the preparation station are
296 baked out at 40-50 °C with the help of the installed heaters. After milling, the cryo-FIB shuttle
297 with the sample is transferred back to the glove box and the autoloader grids are unloaded,
298 rotated by 90° and mounted to the autoloader cassette. Finally, the cassette is loaded into the
299 NanoCab (Thermo Fisher Scientific) and transferred to the electron cryo microscope (Titan
300 Krios, Thermo Fisher Scientific).
301
302 **Cryo-FIB/SEM**
303 The developments described in this study were carried out on an Aquilos cryo-FIB/SEM
304 (Thermo Fisher Scientific), equipped with an additional ion getter pump (Agilent), a larger
305 cryo-shield (manufactured by CryoVac GmbH & Co KG) and stage heater (in-house
306 production). The instrument is also equipped with a gas injection system (GIS) and a platinum
307 sputter coater. After insertion, the grids are coated with an organometallic platinum layer to
308 protect the sample while milling. The sputter coating is utilized to avoid charging effects
309 during imaging in the SEM and can either be done before or after GIS deposition. For scanning
310 electron imaging, an acceleration voltage of 2-5 kV with an electron current of max. 28 pA was
311 used. The ion optics were operated at 30 kV acceleration voltage with different ion currents
312 (50 – 700 pA). All ion currents are specified by the user and should be tuned for every new
313 sample material. The alignment of the ion optics is crucial and was performed at least once a
314 week to avoid massive image shifts while changing the ion currents. For scanning electron
315 imaging, the installed Everhart-Thonley detector was utilized.
316
317 **Automated milling via AutoTEM Cryo**
318 Although the relevant milling parameter as ion beam currents, milling patterns and milling
319 time might vary for different types of sample, a brief overview is given:
320 After the identification of ROIs, there are two possible workflows: 1) The eucentric
321 height and the milling angle are set for each lamella site using the MAPS application (Thermo
322 Fisher Scientific). Typically, this preparation step takes approximately 5 min for each lamella
323 site. Alternatively, 2), After setting the ROI positions in MAPS and then transferring them to

324 AutoTEM Cryo (Thermo Fisher Scientific), the eucentric position, tilts and beam shift values
325 can be set in AutoTEM using the preparation step. This can take around 2-3 minutes per site
326 and has the benefit of storing the beam shifts.
327 In the first milling step, the exact lamella positions were defined and relevant milling
328 parameters were set. The lamella width is mostly defined by the type of sample material and
329 the condition of the specific ROI. Lamella widths of 8 – 10 µm were typically used. The desired
330 lamella thickness was project dependent: in some cases, the project required a lamella
331 thickness below 150 nm and in other cases, a thickness of 250 nm was still within the required
332 limits. For the first estimation of milling times, a total sample thickness of 15 µm was assumed.
333 In the first milling step, the site preparation, relief cuts were milled to release the stress
334 from the support film of the grid, which might occur during plunge freezing. Here, a width of
335 1-3 µm and a height of 10-15 µm were typically used. The relief cuts were milled at relatively
336 high ion beam currents (0.5–1 nA) for approximately 5 min.
337 After site preparation, most of the bulk material was removed during rough milling.
338 This task is separated into four different milling steps. During the first milling step, most of the
339 sample material is ablated with relatively high ion beam currents (0.5–1 nA) until a lamella
340 thickness of approximately 2-3 µm is reached. In the following milling steps, the ion currents
341 were consecutively reduced from 0.5 to 0.1 nA. After these milling steps, the lamellae
342 thickness was already reduced to 300-600 nm. For the initial rough milling the front and rear
343 pattern height were set to 5-7 µm. All later milling pattern were calculated accordingly. Since
344 most of the sample material was removed during rough milling, most of the time was spent
345 during this step (20-30min).
346 The polishing step was executed in up to five successive milling steps with an ion beam
347 current of 30-50 pA. Since most of the sample material was already ablated, the last thinning
348 process took only approximately 5-10 min.
349
350 **Cryo-electron tomography and tomogram reconstruction**
351 All data sets were collected on a Titan Krios (Thermo Fisher), operated at an acceleration
352 voltage of 300kV. The microscope is equipped with a field emission gun, a BioQuantum
353 imaging filter (Gatan, Munich, Germany) with a set energy width of 20eV and a K3 direct
354 electron detector (Gatan, Munich, Germany). The software package SerialEM was used for
355 automated data acquisition [Mastronade2005]. For reconstruction of the tomograms, the

356 software package IMOD was used [Kremer1996]. Imaging conditions are listed in
357 Supplementary Table 2.
358

359 **Template Matching, Polysome Detection and Visualization**

360 Tomograms were binned (IMOD bin 8x, 14.32 Å $pix^{-1}$) and template matching was performed
361 using PyTom [Hrabe2012]. First a reference was constructed from approximately 300
362 manually picked ribosomes, which were aligned in PyTom using the fast-rotational matching
363 (FRM) algorithm. The reference obtained from this was then truncated at the small subunit to
364 allow later removal of false positives. For each tomogram, the 800 highest-scoring cross-
365 correlation peaks were extracted, and the subtomograms aligned and classified using a
366 maximum likelihood approach in Relion 3 [Zivanov2018] to remove false positives. This was
367 judged by the absent small subunit in the false positive class averages. After initial processing
368 at bin 8x, further classification and refinement of the 2x binned (3.58 Å $pix^{-1}$) subtomogram
369 averages was performed in Relion, including normalization and CTF estimation with CTFFIND
370 4.1.5 [Rohou2015]. The final list of particles (approximately 15000) yielded a ribosome
371 structure at 14 Å resolution (0.143 FSC criterion), which was used in all animations. Polysome
372 detection was performed analogously to published using an inhouse Matlab script
373 [Brandt2010].

374

## Figures

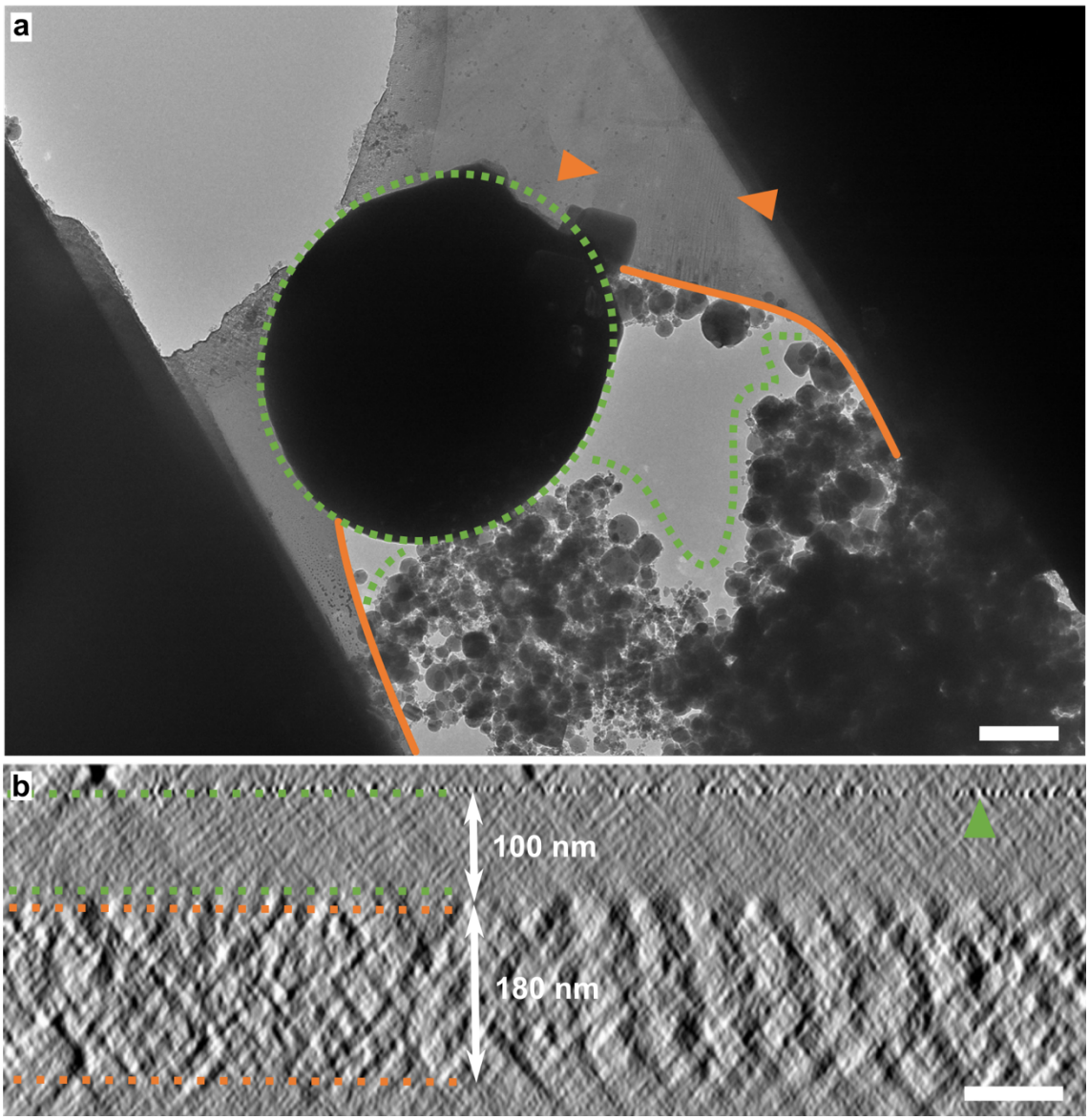


**Figure 1: Possible artefacts arising during handling, transfer and processing.** a) This overview shows a rare case, were all possible artifacts were found on a single lamella. If the sample material is transferred in a hydrous environment, ice crystals of different sizes (highlighted by green dashed lines) can contaminate the lamella. Moreover, the fragile lamella can be easily damaged during handling, and in worst case, cracks across the lamella can appear (orange solid lines). Obviously, data acquisition at the region-of-interest (orange triangles) is impossible in such cases. Scale bar, 1 µm. b) Even if these artefacts can be avoided, intact lamellae can be corrupted by contaminations occurring during milling. The water fraction of the residual gas inside the vacuum chamber deposits by time onto the lamella (green dashed line). As indicated (white arrows), the thickness of the polished lamella was originally 180 nm but due to the water deposition inside the cryo-FIB/SEM, it increased to approximately 280 nm, reducing the quality of the lamella. The water deposition can be identified unambiguously since the lamella was coated with platinum (green triangle) in the end of the milling procedure. Scale bar, 100 nm.

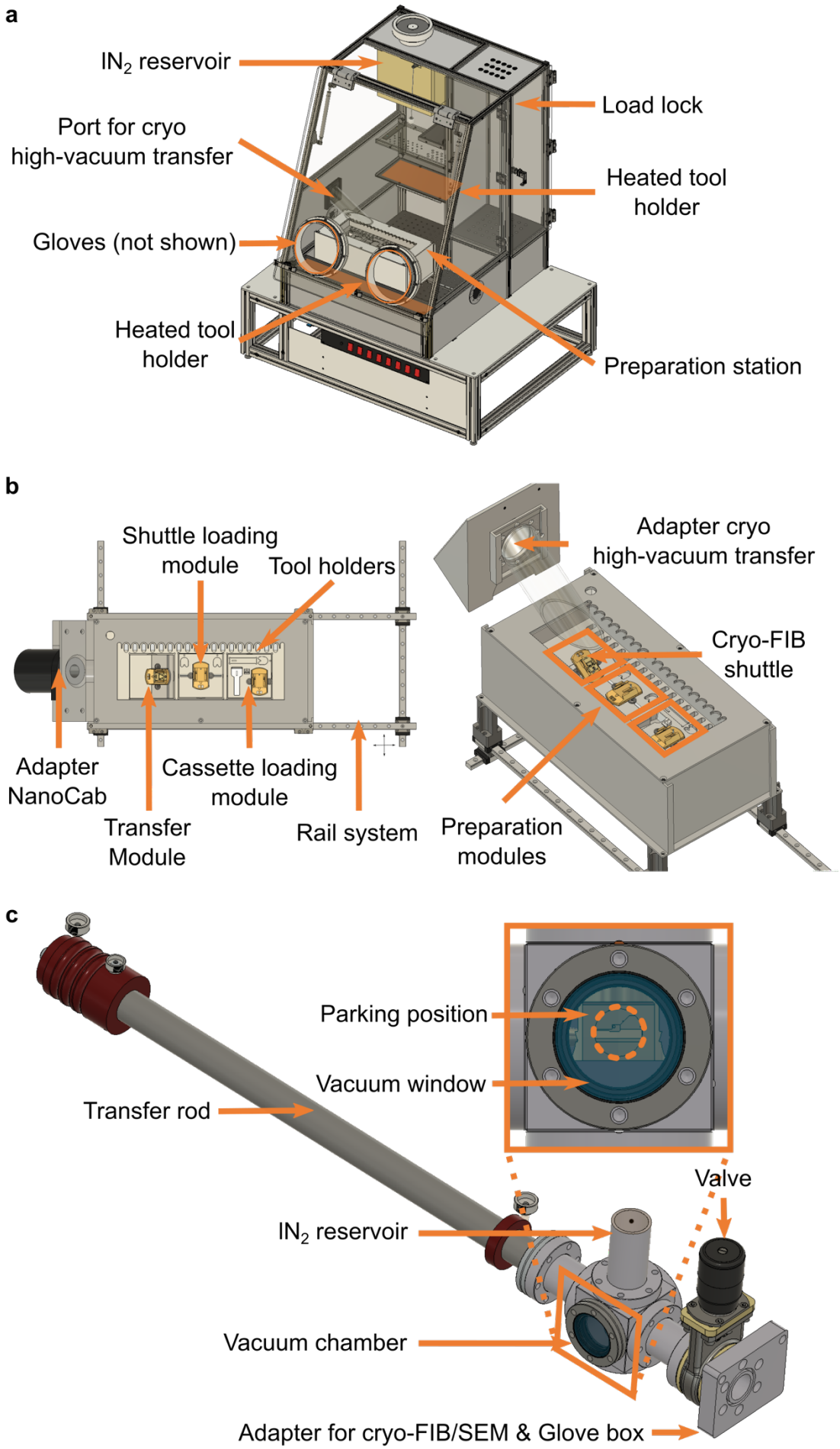
a
IN2 reservoir
Load lock
Port for cryo
high-vacuum transfer
Heated tool
holder
Gloves (not shown)
Heated tool
holder
Preparation station
b
Shuttle loading
module
Tool holders
Adapter cryo
high-vacuum transfer
Cryo-FIB
shuttle
Adapter
NanoCab
Cassette loading
module
Transfer
Module
Rail system
Preparation
modules
c
Parking position
Vacuum window
Transfer rod
Valve
IN2 reservoir
Vacuum chamber
Adapter for cryo-FIB/SEM & Glove box

**Figure 2: Schematic of the glove box, the preparation station, and the high vacuum cryo transfer system.** a) The glove box was designed to enable convenient sample handling in an anhydrous environment. To reduce the humidity to a minimum, the glove box is purged during operation with nitrogen and a cold trap is installed in the back of the $lN_2$ reservoir. $lN_2$ can be taken from this reservoir for applications inside the glove box. For convenient handling, heated tool holders are installed. A load lock enables the insertion of tools without breaking the humidity barrier. b) To guarantee a comfortable and secure handling of the sample material, a new preparation station was developed. The preparation station consists of four parts: the liquid nitrogen bath, the preparation modules, the adapter for the transfer systems and the adapter for the NanoCab. All modules can be re-arranged inside the liquid nitrogen bath according to the preferences of the operator and are designed for left- and right-handed persons. Clipped autoloader C-clip rings can be loaded onto the cryo-FIB shuttle or to the autoloader cassette using the corresponding modules. The preparation station is mounted onto a rail system to ensure highest flexibility inside the glove box. c) The high vacuum cryo transfer system consists of a transfer rod for picking up the cryo-FIB shuttle, a vacuum chamber, liquid nitrogen reservoir, a valve and the adapter for the cryo-FIB/SEM and glove box. The sample can be picked up by the transfer rod and is inserted in the vacuum chamber. Inside the vacuum chamber the cryo-FIB shuttle is placed in a parking position. Here, the shuttle is actively cooled by the $lN_2$ reservoir. The liquid nitrogen acts also as a cryo-pump and maintains the vacuum level, while the high vacuum cryo transfer is disconnected from the pumps. The $lN_2$ volume holds for approximately 30 min. After the shuttle is positioned in the parking position, the valve towards the glove box is closed and the high vacuum cryo transfer is evacuated. Thereafter, the valve at the transfer system is closed and the sample can be transferred to the cryo-FIB/SEM.

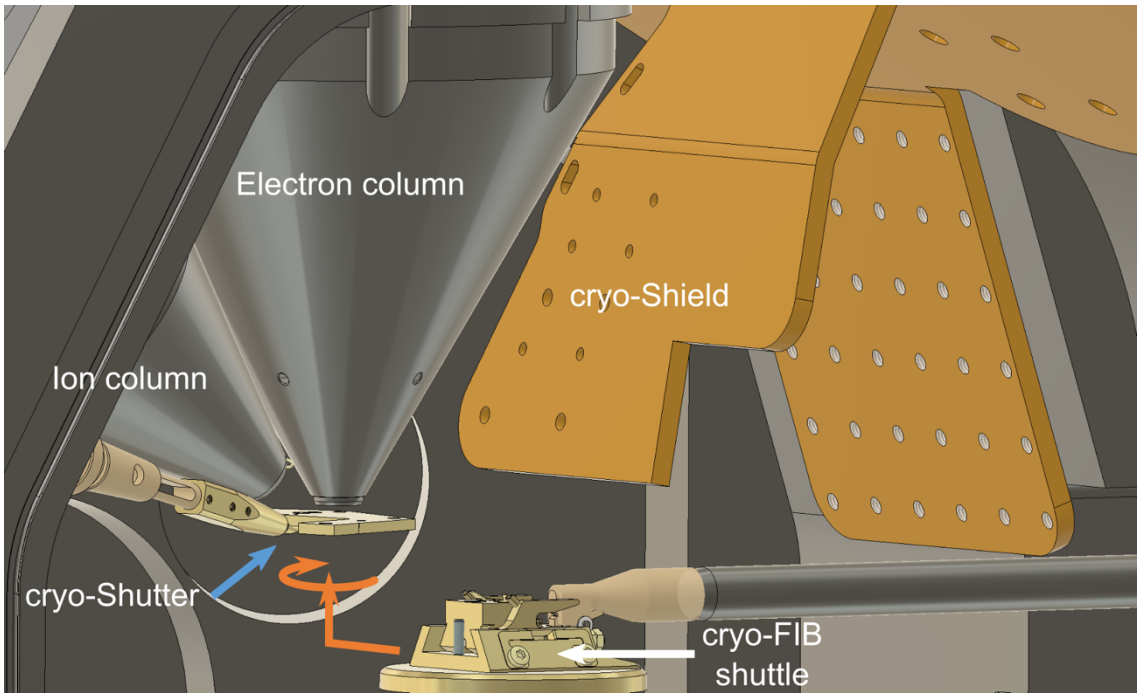


**Figure 3: Schematic of the cryo-shield and cryo-shutter**. The total surface area of the cryo-shield is approximately 880 $cm^2$. Assuming a pumping speed of 15 l $cm^{-2}$ $s^{-1}$ [Bello2017], the total pumping speed can be estimated to be 13,000 l $s^{-1}$. To reduce the partial pressure in the vicinity of the sample even further, a cryo-shutter can be inserted during milling (blue arrow). The cryo-shutter covers most of the grid and in combination with the installed stage heater (not shown), the contamination rate decreases to 5.7 nm $h^{-1}$. With these improvements, the sample can be prepared and stored in the milling position (orange arrows) until imaging without major water deposition.

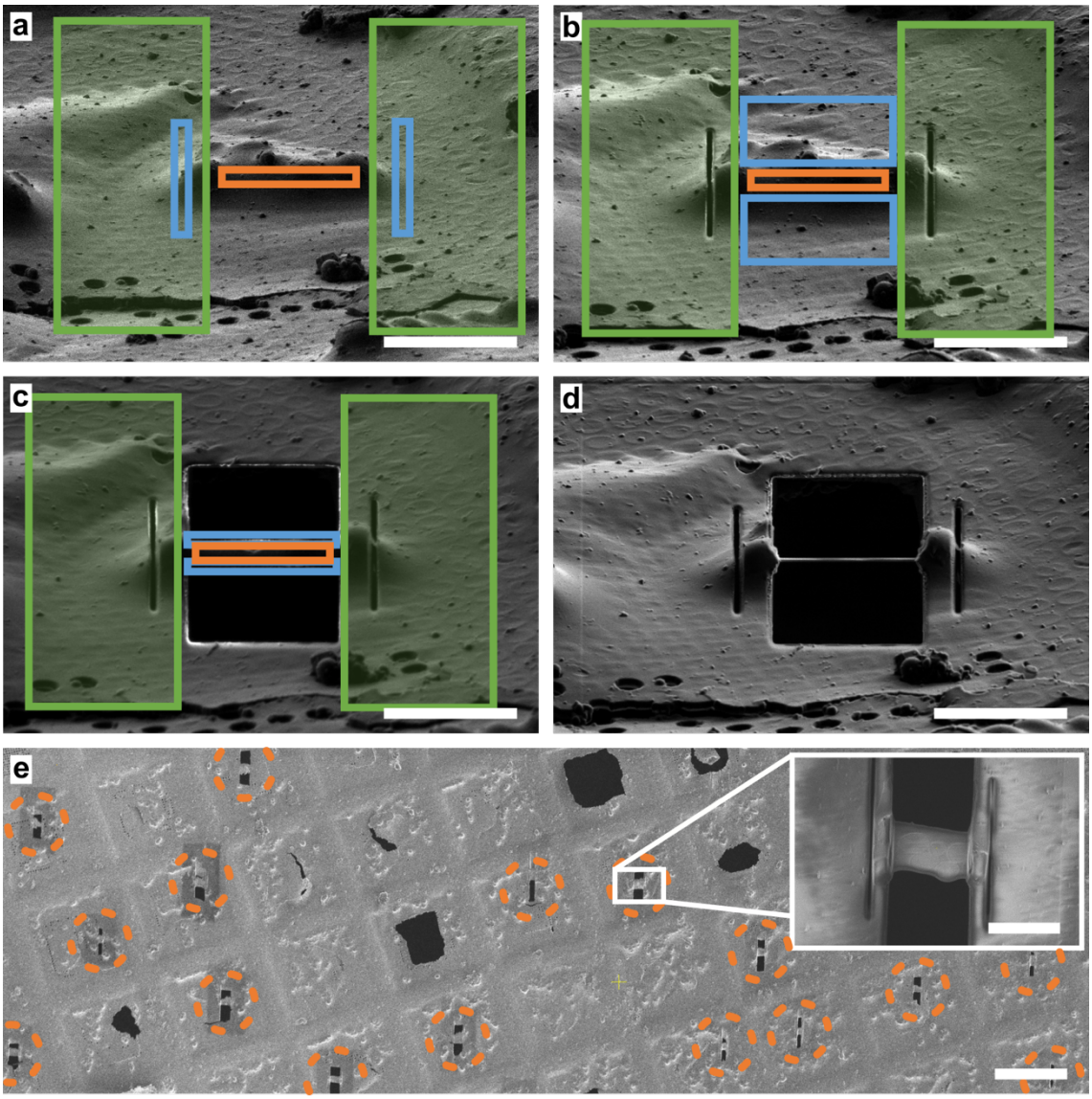


**Figure 4: AutoTEM pipeline for automated lamellae preparation.** a) After the lamella site is centered, micro-expansion joints (blue frame) are milled next to the lamella site to release possible stress of the support layer. Scale bar, 10 µm. b) Thereafter, rough milling (blue frame) is performed in four consecutive steps. First, the bulk material is ablated with relatively high currents (0.5 – 1 nA). In the subsequent steps, the lamella is thinned to a thickness between 250 – 500 nm with an ion current of 0.5 to 0.1 nA. Scale bar, 10 µm. c) In the last step, the lamella is polished (blue frame) with low ion beam currents (30 – 50 pA). Scale bar, 10 µm. In order to correct for possible stage drifts, specific regions of the ROI (green frames in a), b) and c)) are imaged frequently and compared by a newly developed, cross-correlation based algorithm. d) The final lamella thickness is optimally about 100 to 200 nm. Scale bar, 10 µm. e) Overview of the different lamella sites, prepared during the same session (dashed orange circles). Scale bar, 50 µm (Inset scale bar: 10 µm).

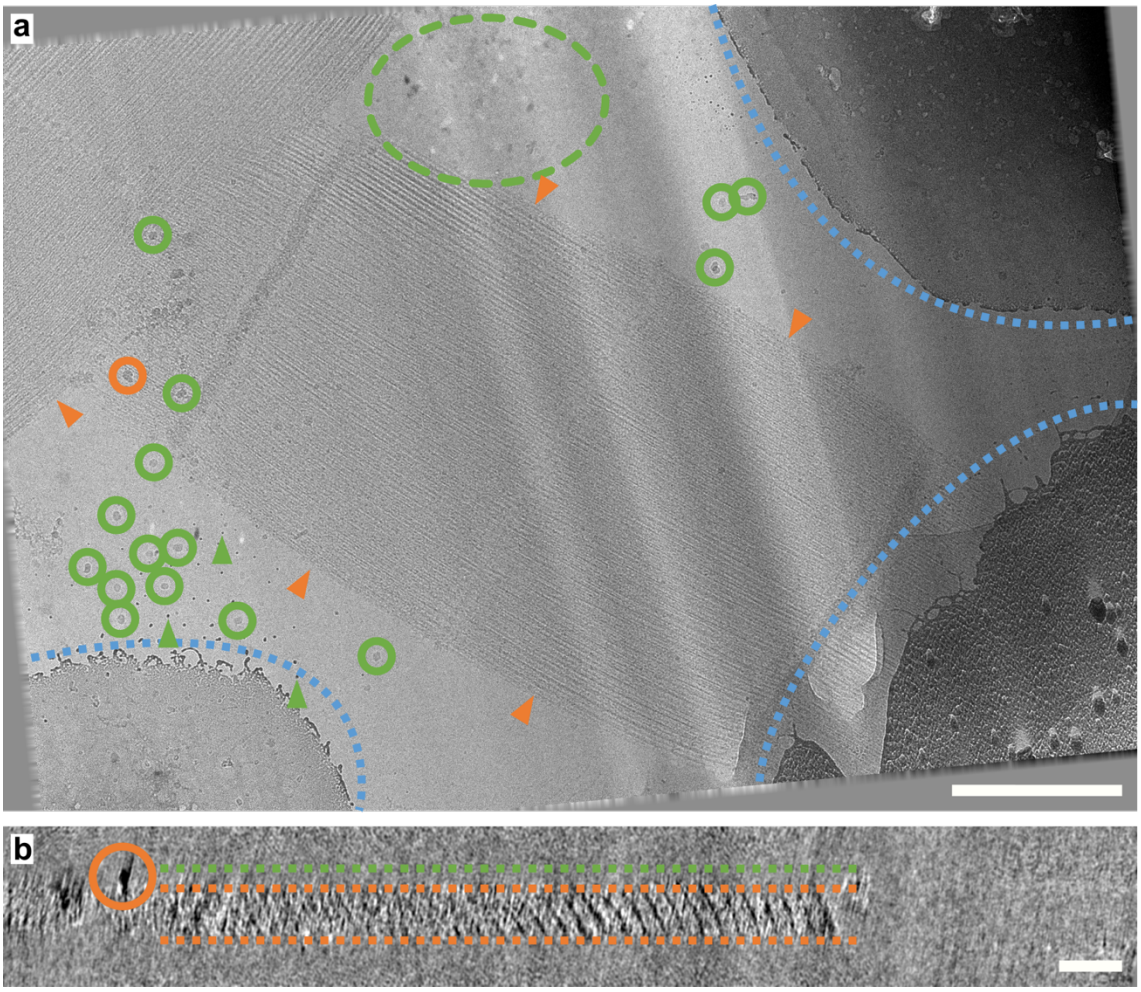


**Figure 5: Quality assessment of the pre- and post-processing step.** a) Overview of a lamella. The lamella is only covered with small ice crystals (green circles) which do not prevent data acquisition in these areas. Areas of the residual platinum layer can be identified (blue dashed line). Although these areas should not be used for data acquisition, the useable area was large enough to take six tomograms. In some areas, non-vitrified regions can be identified (green dashed eclipse) but within the region of interest (orange triangles), no crystalline ice can be found. Scale bar: 1 µm. b) Orthogonal slice through the tomogram shown in a). The average thickness is approximately 280 nm (orange dashed line). The lamella was stored approximately 30 min in the cryo-FIB/SEM prior to imaging. The green dashed line indicates the theoretical contamination layer, which would have deposit on the lamella without the introduced hardware modifications. As indicated by the orange circle (see also orange circle in a)), the ice contamination is in direct proximity to the lamella. This shows that the contamination rate is reduced. The slice was Gauss filtered and averaged (6 slices). Scale bar: 300 nm.

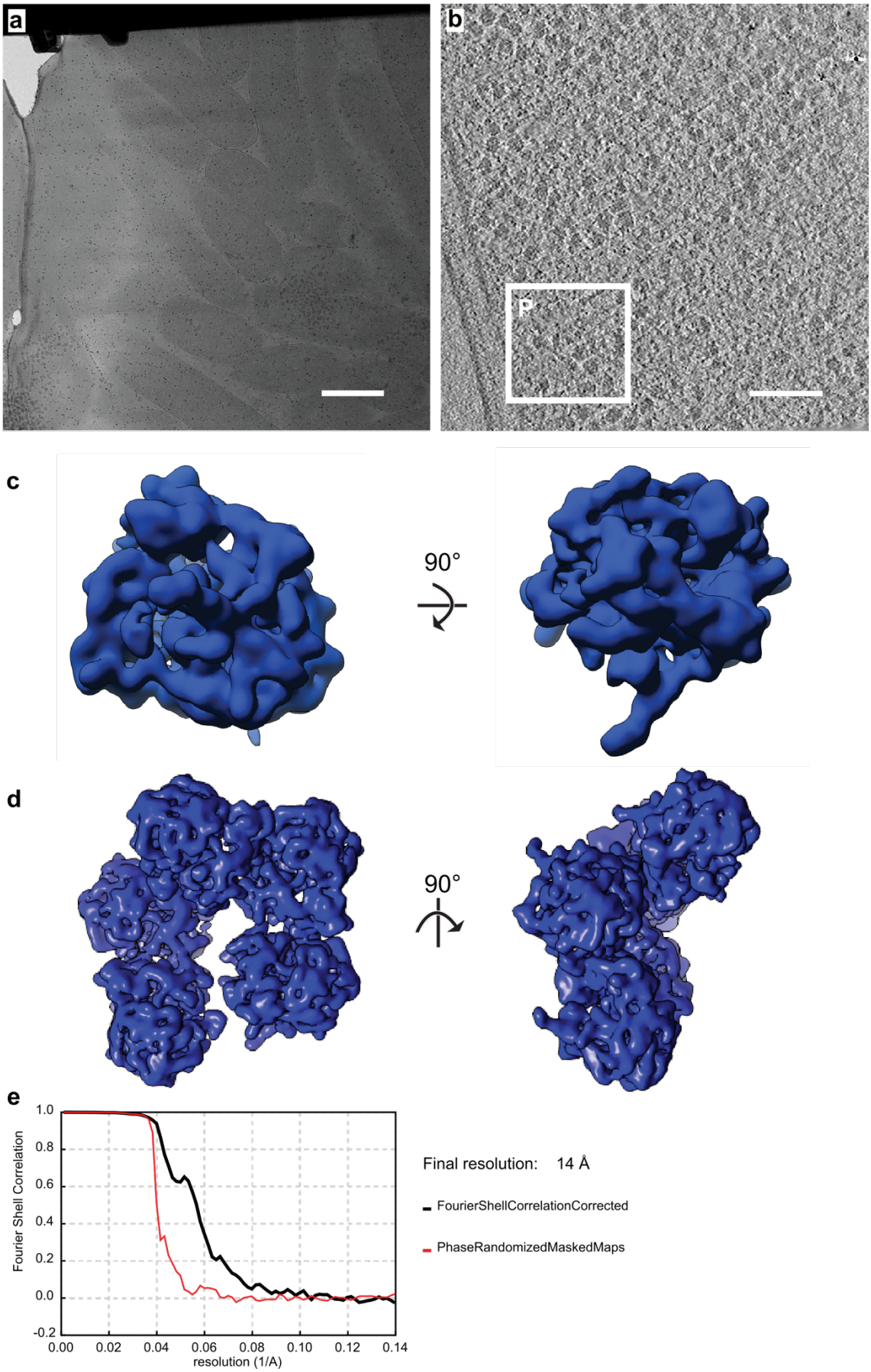


**Figure 6: Suitability of automatically milled lamellae for subtomogram averaging.** a) Representative overview of an automatically milled lamella. The lamella was sputter coated

458 to reduce charging artefacts. Scale bar: 2.5 µm. b) Macromolecular complexes such as
459 ribosomes are readily detectable. Scale bar: 100 nm. c) Subtomograms can be averaged to
460 high resolution (14 Å at 0.143 FSC criterion). d) Additionally, orientations and locations can be
461 precisely determined, which enabled the detection of polysomes up to a pentamer (insert and
462 boxed region P in a)).

463

464

| **Sample** | **Number of ROI (lamellae sites)** | **Number of successfully roughly milled lamellae** | **Number of successfully polished lamellae** |
|---|---|---|---|
| Myofibrils | 21 | 20 | 10 |
| A9 cells | 7 | 6 | 6 |
| *S. cerevisiae* | 94 | 89 | 85 |
| *E. coli* | 23 | 23 | 21 |
| Neurons | 3 | 3 | 2 |
| HeLa cells | 6 | 6 | 6 |
| Sum | 154 | 147 | 130 |
| **Success rate** | | **95%** | **88%** |

465

466 **Table 1: Milling statistics for different types of sample material using the automated**
467 **lamella production pipeline.**

468

| Step in workflow | Possible contamination | Implication | Current technology/ limitations | New technology/ improvements |
|---|---|---|---|---|
| **Sample Vitrification** | Ice particles | Lack of visibility of sample surface | Air-dehumidified rooms | Not addressed |
| **Cryo-FIB/SEM Loading** | Ice particles and condensation | Lack of visibility and curtaining | Aquilos loading station:<br><br>No regulated environment<br>Limited runtime (~ 1 h) | Glove Box, preparation station, high vacuum cryo transfer:<br>Anhydrous environment<br>Extended runtime (> 3 h) |
| **Cryo-FIB/SEM Milling** | Condensation | Increased thickness of lamella | Cryo-shielding:<br><br>Contamination rate ~ 50 nm $h^{-1}$<br>Limit of throughput | Extra shielding, cryo-shutter, stage heater:<br>Contamination rate ~ 6 nm $h^{-1}$<br>High throughput |
| **Cryo-FIB/SEM Unloading** | Ice particles and condensation | Increased thickness of lamella | Aquilos loading station:<br><br>No regulated environment<br>Limited runtime (~ 1 h)<br>Cassette loading not possible | Glove Box, preparation station, high vacuum cryo transfer:<br>Anhydrous environment<br>Extended runtime (> 3 h)<br>Cassette loading possible |
| **Sample Storage** | Ice particles | Loss of viewable areas | Grid box and Dewar | Not addressed |

**Table 2: Overview of the improvements of the cryo-FIB/SEM workflow**

471 **References**

472

473 [Grange2017] Grange, M, Vasishtan, D., & Grünewald, K. Cellular electron cryo tomography
474 and in situ sub-volume averaging reveal the context of microtubule-based processes. *J. Struct.*
475 *Biol.* **197**, 181-190 (2017).

476

477 [Bartesaghi2012] Bartesaghi A. et al. Secondary Structure Determination by Constrained
478 Single-Particle Cryo-Electron Tomography. *Structure* **20**, 2003-2013 (2012).

479

480 [Schur2016] Schur, F. K. M. et al. An atomic model of HIV-1 capsid-SP1 reveals structures
481 regulating assembly and maturation. *Science* **353**, 506-508 (2016).

482

483 [Vulovic2013] Vulovic, M. et al. Image formation modelling in cryo-electron microscopy. *J.*
484 *Struct. Biol.* **183**, 19-32 (2013).

485

486 [Al-Amoudi2004] Al-Alamoudi, A., Norlen, L.P.O., & Dubochet J. Cryo-electron microscopy of
487 vitreous sections of native biological cells and tissues. *J. Struct. Biol.* **148**, 131-135 (2004)

488

489 [Al-Amoudi2005] Al-Alamoudi, A., Studer, D. & Dubochet, J. Cutting artefacts and cutting
490 process in vitreous sections for cryo-electron microscopy. *J. Struct. Biol.* **150**, 109-121 (2005).

491

492 [Marko2007] Marko, M. et al. Focused-ion-beam thinning of frozen-hydrated biological
493 specimens for cryo-electron microscopy. *Nat. Methods* **4**, 215-217 (2007).

494

495 [Rigort2010] Rigort, A. et al. Micromachining tools and correlative approaches for cellular
496 cryo-electron tomography. *J. Struct. Biol.* **172**, 169-179 (2010).

497

498 [Hagen2015] Hagen C. et al. Structural basis of vesicle formation at the inner nuclear
499 membrane. *Cell* **163** 1692-1701 (2015).

500

501 [Mahamid2016] Mahamid J. et al Visualizing the molecular sociology at the HeLa cell nuclear
502 periphery. *Science* **351**, 969–972 (2016).

[Medeiros2018] Medeiros, J.M. et al. Robust workflow and instrumentation for cryo-focused ion beam milling of samples for electron cryotomography. *Ultramicroscopy* **190**, 1-11 (2018).

[Tacke016] Tacke, S. et al. A Versatile High-Vacuum Cryo-transfer System for Cryo-microscopy and Analytics. *Biophysical Journal* **110** 4, 758-765 (2016).

[Echlin1992] Echling, P. Low-Temperature Microscopy and Analysis. Plenum Publishing Corporation, New York (1992)

[Umrath1983] Umrath, W.W. Berechnung von Gefriertrocknungszeiten für die elektronenmikroskopische Präparation. *Mikroskopie* **40**, 9-34 (1983).

[Wolff2019] Wolff, G. Mind the gap: Micro-expansion joints drastically decrease the bending of FIB-milled cryo-lamellae. *J. Struct. Biol*. In Press (2019).

[Schaffer2017] Schaffer, M. et al. Optimized cryo-focused ion beam sample preparation aimed at in situ structural studies of membrane proteins. *J. Struct. Biol.* **197**, 73-82 (2017).

[Mastronade2005] Mastronarde D.N. Automated electron microscope tomography using robust prediction of specimen movements. *J. Struct. Biol.* 152, 36–51 (2005).

[Hrabe2012] Hrabe, T. et al. PyTom: a python-based toolbox for localization of macromolecules in cryo-electron tomograms and subtomogram analysis. *J. Struct. Biol.* **178**, 177-188 (2012).

[Zivanov2018] Zivanov, J. et al. New tools for automated high-resolution cryo-EM structure determination in RELION-3. *eLife* **7**, e42166 (2018).

[Rohou2015] Rohou, A. and N. Grigorieff, CTFFIND4: Fast and accurate defocus estimation from electron micrographs. *J. Struct. Biol.* **192**, 216-221 (2015).

[Brandt2010] Brandt, F. et al. The Three-Dimensional Organization of Polyribosomes in Intact Human Cells. *Mol. Cell* **39**, 560-569 (2010).

[Kremer1996] Kremer, J.R., Mastronarde, D.N. & McIntosh, J.R. Computer visualization of three-dimensional image data using IMOD. *J. Struct. Biol.* **116**, 1-6 (1996).

[Bello2017] Bello, I. Vacuum and Ultravacuum: Physics and Technology. CRC Press (2017)

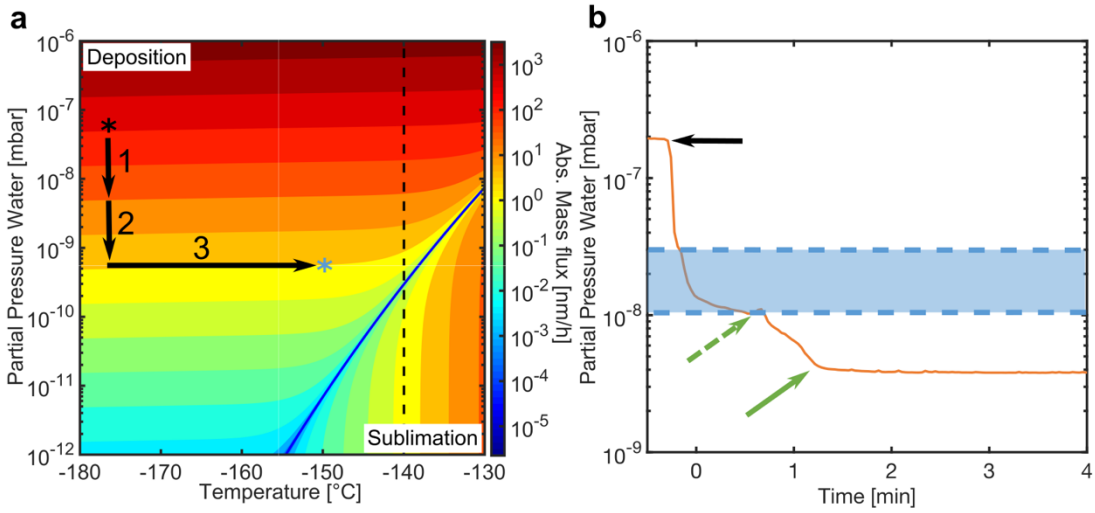


**Supplementary Figure 1: Phase diagram of water.** a) Phase diagram of water and the associated mass flux (deposition/sublimation). The dashed line indicates the devitrification temperature of water. The black asterisk marks the partial pressure value of the cryo-FIB/SEM before the hardware modifications. The arrows indicate the used strategy to minimize the ice deposition onto the sample. By the installation of the cryo-shield, the partial pressure of water dropped to 3 x $10^{-9}$ mbar (black arrow 1) and the contamination rate decreased to (72 +/- 4) nm $h^{-1}$. If the cryo-shutter is inserted, the partial pressure in the vicinity of the sample decreases by approximately one order of magnitude (black arrow 2), which reduces the contamination rate to (12.8 +/- 1.6) nm $h^{-1}$. To reduce the contamination rate even more, the sample is heated to approximately -150°C (black arrow 3). Herewith, the contamination rate is reduced to (5.6 +/- 1.0) nm $h^{-1}$ (blue asterisk). b) Partial pressure of water inside the cryo-FIB/SEM chamber measured during operation (orange graph). As soon as the cryo-shield is cooled (black arrow), water molecules from the residual gas get trapped and the partial pressure decreases. After 30 min, the system reaches its final pressure value (solid green arrow). The impact of the cryo-shield is indicated by the green dashed arrow. At this time point, the cryo-stage reached already -185°C and the cryo-shield temperature was still above -100°C, where the pumping speed of the cryo-shield is negligible. As indicated by the blue area, this value matches with the partial pressure regime of standard cryo-FIB/SEM instruments.

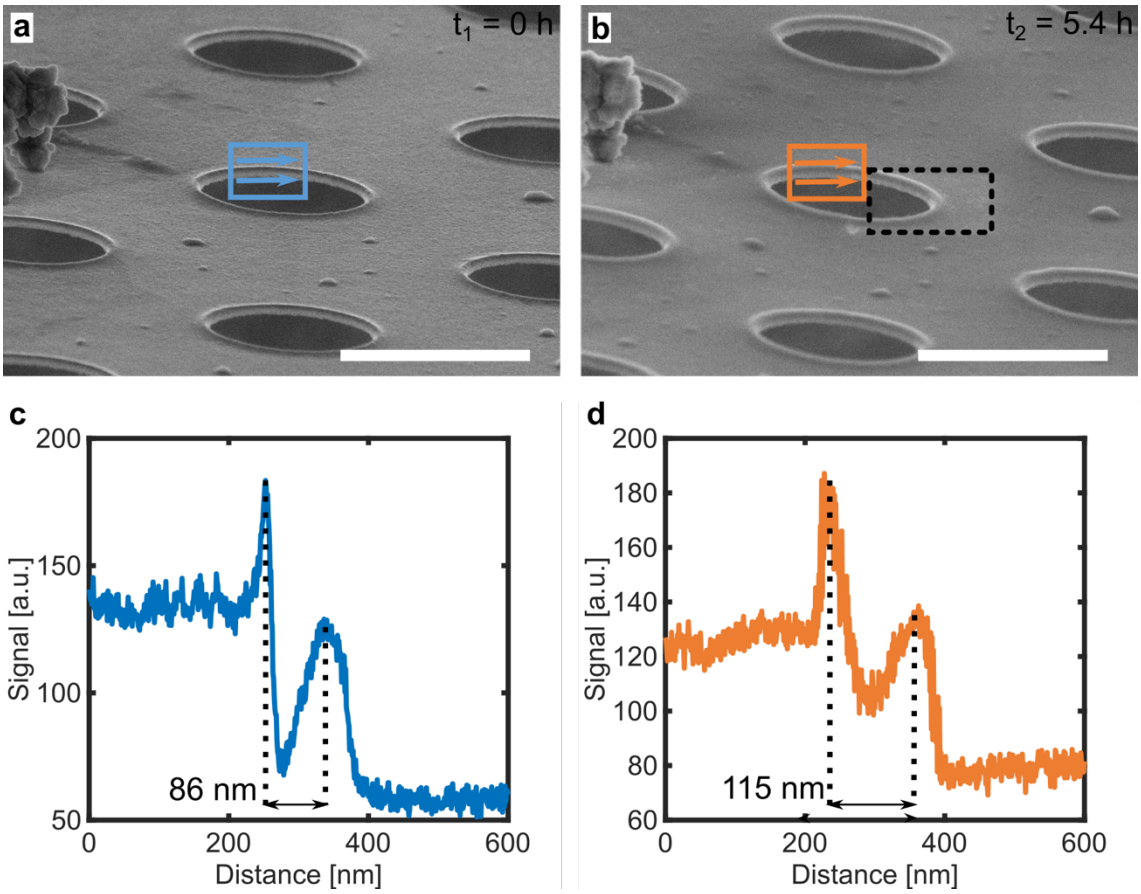


**Supplementary Figure 2: Contamination rate measurement in the milling position.** a) Before imaging, the stage, cryo-shield and the cryo-shutter were cooled. After reaching the final temperature of approximately -185°C, the stage was heated to -165°C. Since there might be a temperature offset of 15°C between stage and shuttle, we assume that the sample has a temperature of -150°C. Whereas the cryo-shield reached a temperature of -185°C, the cryo-shutter could only be cooled to -177°C. To determine the contamination rate in the milling position, a holey gold EM grid (UltraAuFoil holey gold grid) was mounted to the cryo-FIB/SEM shuttle and loaded into the instrument. For the baseline measurements ($t_1$) the thickness of the holey gold film was determined (blue frame). To avoid ice ablation during focusing, beam tuning was done next to the region-of-interest (black frame). b) After 5.4 hours ($t_2$), another series of thickness measurement was performed on the same holes. c) Baseline measurements: Line profiles were averaged horizontally (blue arrows in a)). The upper and the lower edge of the profile (dotted black line) were fitted with Gaussian function. If fitting was not possible, edge positions were determined manually. The centers of the edges were used to calculate the thickness. d) Thickness determination after 5.4 h: The line profile was averaged and the thickness was determined as described in c). Finally, both values were corrected regarding the tilting angle of the grid and the total increase in thickness was determined. Herewith, the contamination rate can be calculated. Scale bars, 2 µm.

a

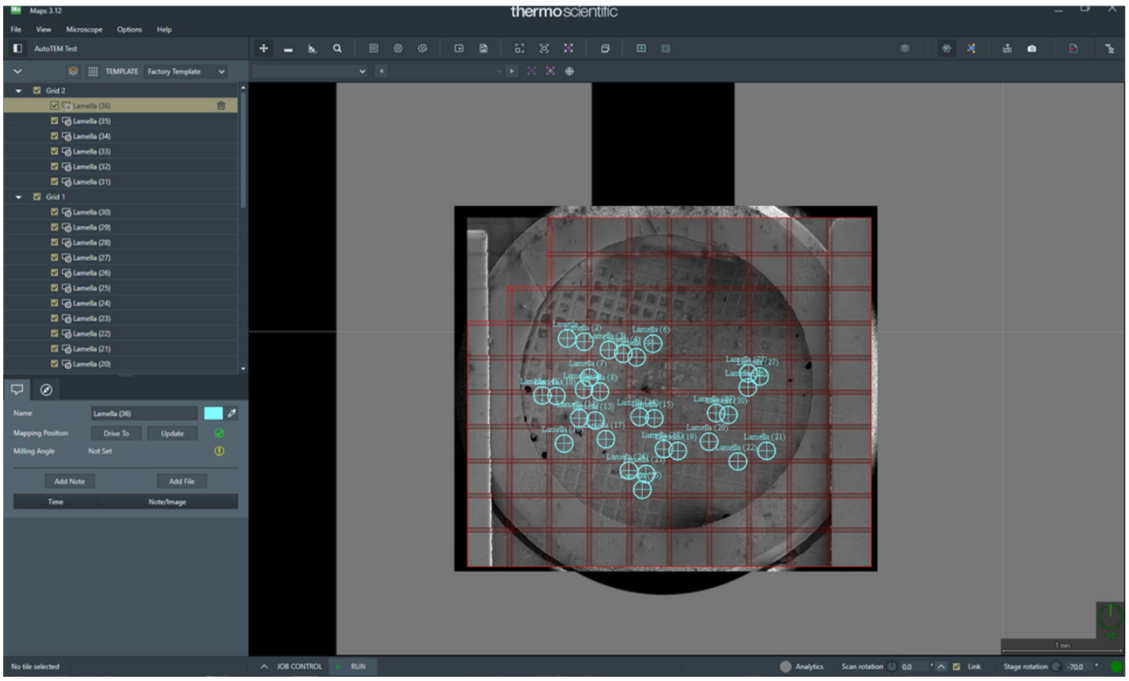


b

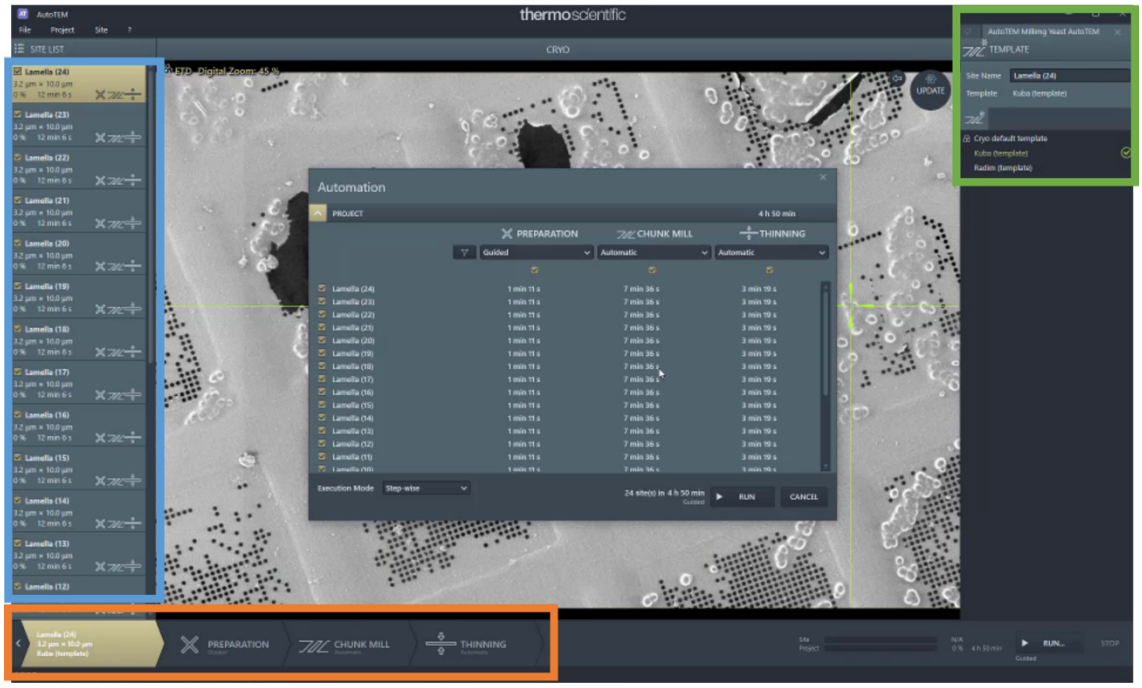


**Supplementary Figure 3: Software applications.** a) Overview of the MAPS software application. Either ROIs are identified by light cryo microscopy and uploaded in the MAPS software or identified directly in the overview image as shown here. b) Overview of the AutoTEM Cryo software application. The software pipeline is separated into three different tasks (orange frame): i) Site preparation, ii) rough milling iii) thinning. Each step consists of several sub-tasks (green frame) which can be tuned to guarantee an optimal performance for each lamella site (blue frame).

| Stage temperature [°C] | Shield temperature [°C] | Status shutter | Contamination rate [nm $h^{-1}$] (n) |
|---|---|---|---|
| -188 | RT | Not inserted | 85 ± 7 (15) |
| -188 | -177 | Not inserted | 72 ± 4 (8) |
| -188 | -177 | Inserted | 12.8 ± 1.6 (15) |
| -165 | -177 | Inserted | 5.6 ± 1.0 (15) |

591

592 **Supplementary Table 1: Influence of the different hardware components on the**
593 **contamination rate inside the cryo-FIB/SEM.** The number of holes, which were used for
594 thickness determination (sample size), is given by the number n. For each condition, two to
595 three positions, containing at least four holes, were selected. All measurements of one
596 condition were performed on the same day. The uncertainty is estimated by the standard
597 deviation of the different conditions.

598
599

| Sample | Defocus [µm] | Tilting range [°] | Increments [°] | Pixel size [Å] | Total Dose [$e^-$/Å] |
|---|---|---|---|---|---|
| **Myofibrils overview** | 20 | -29 to 39 dose symmetric | 2 | 11.3 | 17 |
| ***E. coli* overview** | 50 | 0 | 0 | 22.8 | 10 |
| ***E. coli* tomograms** | 1.5-3.5 | ± 60 dose symmetric | 3 | 1.79 | 120 |

600

601 **Supplementary Table 2: Imaging conditions for the presented data.** The imaging conditions
602 for the two tomogram slices (shown in Figure 5a,b and Figure 6b) and the TEM image (shown
603 in Figure 6a) are listed.

604

605